scientific reports

Check for updates

OPEN

Pure thermal spin current and perfect spin-filtering with negative differential thermoelectric resistance induced by proximity effect in graphene/silicene junctions

Zainab Gholami & Farhad Khoeini✉

The spin-dependent Seebeck effect (SDSE) and thermal spin-filtering effect (SFE) are now considered as the essential aspects of the spin caloritronics, which can efficiently explore the relationships between the spin and heat transport in the materials. However, there is still a challenge to get a thermally-induced spin current with no thermal electron current. This paper aims to numerically investigate the spin-dependent transport properties in hybrid graphene/silicene nanoribbons (GSNRs), using the nonequilibrium Green's function method. The effects of temperature gradient between the left and right leads, the ferromagnetic exchange field, and the local external electric fields are also included. The results showed that the spin-up and spin-down currents are produced and flow in opposite directions with almost equal magnitudes. This evidently shows that the carrier transport is dominated by the thermal spin current, whereas the thermal electron current is almost disappeared. A pure thermal spin current with the finite threshold temperatures can be obtained by modulating the temperature, and a negative differential thermoelectric resistance is obtained for the thermal electron current. A nearly zero charge thermopower is also obtained, which further demonstrates the emergence of the SDSE. The response of the hybrid system is then varied by changing the magnitudes of the ferromagnetic exchange field and local external electric fields. Thus, a nearly perfect SFE can be observed at room temperature, whereas the spin polarization efficiency is reached up to 99%. It is believed that the results obtained from this study can be useful to well understand the inspiring thermospin phenomena, and to enhance the spin caloritronics material with lower energy consumption.

The spin caloritronics has now constructed the subject of many researches in recent years[1–3]. Spin caloritonics combines the spintronics[4–6] and thermoelectrics to study the interactions among spin and charge in the presence of temperature bias. It can also provide many different approaches for the thermoelectric waste heat recovery, future information, and device technologies[7–9]. The spin caloritronics usually show different innovative effects such as the SDSE[10], spin Seebeck diode (SSD) effect[11], thermal SFE[12], and the thermal giant magnetoresistance phenomenon[13]. According to the experimental results, the spin Seebeck effect (SSE) initially showed an interaction between the spin and heat currents in the magnetic metals, simultaneously[14]. Thus, there is SSE in different magnetic phases such as ferromagnetic metals, semiconductors, and insulators[15–17], paramagnetic and antiferromagnetic materials[18,19], and nonmagnetic materials if a magnetic field is applied[20]. It is worth mentioning that SDSE and SSE phenomena are both induced due to the interaction between the spin and heat currents. However, the magnons are the carriers in SSE, whereas they are the electrons in SDSE.

In SDSE, the temperature bias can generate a spin current, as an essential physical quantity in spintronics, and provide an efficient way for controlling the electron spins in the presence of the temperature gradient. Since the electron current is often accompanied by Joule heating, the spin current in the low-power-consumption

Department of Physics, University of Zanjan, P.O. Box 45195-313, Zanjan, Iran. ✉email: khoeini@znu.ac.ir

nanodevices is required to be used while the electron current is decreased as much as possible. This is now achievable by SDSE. As shown in the previous studies[21], the spin current may be produced by the opposite current direction for different spins. An almost non-dissipative SDSE can be obtained if the electrons in two spin channels, spin-up and spin-down flow in opposite directions with equal values, which is called the perfect SDSE[22]. It is noted that an essential factor in producing the spin current using a temperature gradient is to find a suitable spin-thermoelectric material, which can keep the spin thermopower with opposite signs for different spins[23].

The Graphene (GE), as the first isolated two-dimensional (2D) material, is composed of a honeycomb structure of carbon atoms, and have widely become popular among researchers. GE often shows different thermal[24,25], mechanical[26,27] and optical[28] properties. However, GE has uncommon transport properties, which are related to its unusual electronic structure[29,30]. This is especially true around the Fermi level, where the charge carriers behave similar to massless particles. Because of the long spin relaxation time and length properties of the GE, it is identified as a promising candidate for the future nanoelectronic and spintronic applications[31]. The magnetic and thermoelectric properties of GE have also attracted great interest in recent years. Some of the applications of this material have already been proposed and discussed in[32,33].

Owing to successful studies of GE, some serious attempts have been made by researchers to develop new forms of low-dimensional materials. More recently, Silicene (SE), a hexagonal atomic structure with silicon atoms two-dimensionally bonded together, was first theoretically developed in the literature[34]. SE was then fabricated by depositing Si on Ag[35], and Ir[36] surfaces in the laboratory environment. The structural stability of the SE was then confirmed by other researchers using the phonon spectra calculations[37]. SE and GE have similar electronic structures near the Fermi level and hence can result in the massless Dirac fermions[38]. This concept is now widely used for developing the high-performance field-effect transistors[39]. One of the properties of SE is that it has a larger bandgap, induced by the spin–orbit interaction (SOI). This establishes the quantum spin Hall effect[40], and has a significant role in spin transport and spintronic devices. The bandgap in SE can be opened and controlled by applying an external electric field normal to the atomic plane[41]. However, GE has not such a property. There is also the interaction between the electromagnetic field and spin–orbit coupling in the SE, a feature that can be used to study physics in quantum phase transition[42]. More recently, several studies have been carried out by researchers to investigate the charge and spin thermal transport properties of the SE[43–45].

As shown in the previous studies (e.g.,[46]), the SDSE can emerge in the graphene-based nanodevices. However, because GE shows an extremely low figure of merit[47], it was introduced as an inefficient thermoelectric material in the next researches[48]. Hence, GE rarely shows a perfect SDSE. On the other hand, the SE may be a more promising material than GE in thermoelectrics. The previous works showed that SE could significantly improve the Seebeck coefficient[49] due to its nonzero energy gap. SE also has some special properties in thermoelectric. For instance, the spin-dependent thermoelectric transport properties of the zigzag SE nanoribbons (ZSNRs) have been studied. The results showed that these ZSNRs could show a high spin-filter efficiency[50]. Another type of ZSNRs was then studied[10] and a perfect SDSE has been observed. The theoretical studies showed that the quasi-one-dimensional wire can provide more significant thermoelectric properties than those of 2D structures[51]. This may be related to the significant changes in the electronic and thermal properties of the material. It is worth mentioning that the thermoelectric properties of the nanostructures can be further improved by different modifications such as hybridization[52], doping[53], absorption[54], and so on. The past theoretical studies showed that the hybrid nanostructures such as hybrid MoS_2/WS_2[55] and BN/GE nanoribbons[56] have higher thermoelectric properties than single nanostructures. In recent years, lateral and vertical GE/SE heterojunctions have theoretically[57–59] and experimentally[60,61] been studied. The results showed that the hybrid systems composed of GE and a different 2D material[62,63] (e.g., SE) could remarkably help to produce a structural type with different properties and applications. However, there is now lack of data about the spin transport, electronic behavior, and thermoelectric properties of the hybrid GSNRs, and further studies are still required in this field.

In this paper, the electronic and thermal spin-dependent transport properties of the hybrid GSNRs are numerically investigated. Besides, in this study, the tight-binding (TB) approach based on the nonequilibrium Green's function (NEGF) method is used. The effects of ferromagnetic exchange field, together with the local external electric fields, are also included. A practical way is then proposed to achieve the SDSE, SFE, and negative differential thermoelectric resistance (NDTR) in the hybrid GSNRs. The main findings of the current study are reported and discussed in two separate sections, including (1) SDSE and (2) SFE. In the SDSE case, the spin-up and spin-down currents with almost equal magnitudes are produced in opposite directions (i.e., nearly perfect SDSE) if a temperature gradient is created between the left and right leads. It is noted that because the spin-polarized conduction electrons are the carriers, thus the results reported in this research are limited to SDSE the phenomenon. A nearly pure spin with very small charge thermopower is also observed. However, the spin polarization has reached up to 99% in the SFE case. It is noted that because of the competition between the spin-dependent currents, some interesting transport features such as the change of the flowing direction and NDTR is observed. This evidently confirms its potential thermoelectric device applications by selecting various device temperature sets.

Models and theoretical calculations

Device structure. The SE atoms have an in-plane distance of 2.30 Å, which is much larger than the bond length of GE, i.e., 1.42 Å. In addition, the next-nearest-neighbor distance in the GE is equal to 2.46 Å, which is almost 7% larger than the in-plane atomic distance of SE. Thus, the construction of a lattice-matched one-dimensional interface between the GE and SE is impossible along the same chirality[58]. On the other hand, there is a small out-of-plane buckling in the SE, and thus it is not located in a plane[42]. To consider this buckling feature, the Si atoms in the GE/SE nanocomposite are first oriented in an out-of-plane mode with two parallel sublattices *A* and *B* vertically separated by a distance of 0.46 Å. The interface is then established via extending the SE by 7%

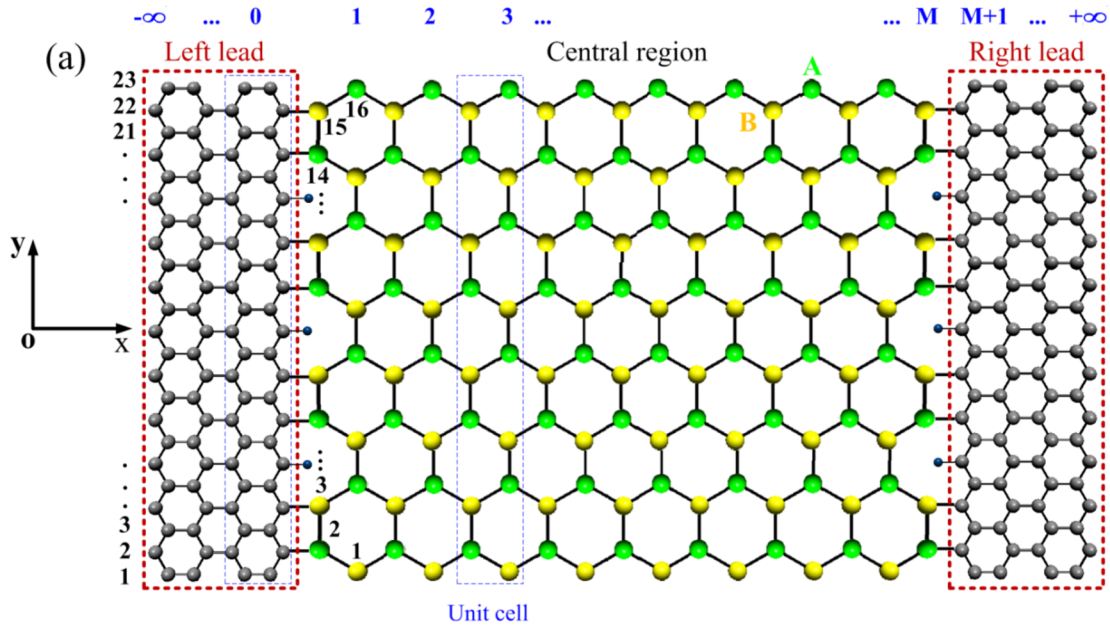

Figure 1. (**a**) A schematic representation of the hybrid graphene/silicene nanoribbon (GSNR) adopted for this study, the central region consists of about $M = 8$ unit cells, each has $N_S = 16$ atoms; each unit cell of the leads also has $N_G = 46$ atoms, (**b**) the external electric and ferromagnetic exchange fields applied to the system, where T_L and T_R define the temperature of the left and right leads, respectively.

along the *y* direction to match the lattice of GE. The distance between the C and Si atoms at the interface is equal to 1.80 Å[57]. Figure 1 shows the atomic configuration of the hybrid GSNR selected for this study. As shown in Fig. 1, the hybrid GSNR is constructed using three different parts, including the semi-infinite metallic armchair GE nanoribbons (AGNRs) on the left and right electrodes and a ZSNR in the central region[64]. Some dangling carbon bonds also remain at the GE/SE interface, which can be passivated by an additional hydrogen atom. It is assumed that the length of central region is almost equal to $M = 8$ unit cells. Each unit cell is composed of $N_S = 16$ atoms, leading to a length and width of 29.85 and 25.27 Å, respectively, for the central region. Besides, each unit cell of the left and right leads includes $N_G = 46$ atoms.

Tight-binding and Green's function method. In this subsection, the electronic quantum transport in the quasi-one-dimensional hybrid GSNR structure is studied. As explained earlier, the hybrid GSNR system is in the *xy* plane, and consists of three different regions, including the AGNRs on the left and right leads and a ZSNR in the middle scattering region (see Fig. 1a). The generalized Hamiltonian for the system can be described as follows:

$$H_T = H_L + H_R + H_C + H_{CL} + H_{CR}, \tag{1}$$

in which, $H_{R(L)}$ and H_C represent the Hamiltonian for the isolated right (left) lead and central region, respectively. Using the TB approximation model[40,42,65], the Hamiltonian of the right (left) lead and the central region are obtained as follows:

$$H_{\mathrm{R(L)}} = -t_{\mathrm{R(L)}} \sum_{\langle i,j\rangle,\alpha} c_{i\alpha}^{\dagger} c_{j\alpha} + eE_{y\mathrm{G}} \sum_{i,\alpha} y_{i\mathrm{G}} c_{i\alpha}^{\dagger} c_{i\alpha} + \mathrm{H.c.}, \tag{2}$$

$$H_{\mathrm{C}} = -t_{\mathrm{C}} \sum_{\langle i,j\rangle,\alpha} c_{i\alpha}^{\dagger} c_{j\alpha} + i\frac{\lambda_{so}}{3\sqrt{3}} \sum_{\ll i,j\gg,\alpha,\beta} \upsilon_{ij} c_{i\alpha}^{\dagger} (\sigma_z)_{\alpha\beta} c_{j\beta} + M_z \sum_{i,\alpha} c_{i\alpha}^{\dagger} \sigma_z c_{i\alpha} + elE_z \sum_{i,\alpha} \xi_i c_{i\alpha}^{\dagger} c_{i\alpha} + eE_{y\mathrm{S}} \sum_{i,\alpha} y_{i\mathrm{S}} c_{i\alpha}^{\dagger} c_{i\alpha} + \mathrm{H.c.}, \tag{3}$$

where $t_{\mathrm{R\,(L)}}$ and t_{C} are the hopping energies between the nearest-neighbor atoms in the right (left) lead, and the central region, so their values are equal to 2.66 and 1.60 eV, respectively. $c_{i\alpha}^{\dagger}(c_{i\alpha})$ creates (annihilates) an electron with spin α at atom i. $\langle i,j\rangle$ and $\langle\langle i,j\rangle\rangle$ represent the nearest-neighbor and next-nearest-neighbor pairs, respectively. λ_{so} is the effective SOI parameter and is equal to 3.9 meV for the central region[42]. Due to the weak SOI in the GE[66], the values of λ_{so} and λ_r are assumed equal to zero for the left and right leads. $\boldsymbol{\sigma} = (\sigma_x, \sigma_y, \sigma_z)$ is the Pauli matrix. υ_{ij} is defined as $\upsilon_{ij} = (\boldsymbol{d}_i \times \boldsymbol{d}_j)/|\boldsymbol{d}_i \times \boldsymbol{d}_j|$ where $\boldsymbol{d}_i$ and $\boldsymbol{d}_j$ are the two nearest bonds connecting the next-nearest-neighbors. $\xi_i = +1, -1$ for the sublattices A and B, respectively; and 2 l is the buckling distance for the SE. E_z is also the perpendicular electric field and produces a voltage difference of $2elE_z$ between the two sublattices, where e is the electron charge. This causes the electrons to experience a staggered potential when jumping from a site to its nearest-neighbor. It is worth mentioning that the external electric field can efficiently differentiate the SE from GE. M_z is the ferromagnetic exchange field, which can be produced by the proximity effect of a ferromagnetic material[42]. $E_{y\mathrm{G}}$ and $E_{y\mathrm{S}}$ are the inhomogeneous transverse electric field components along the x direction, applied to the leads and central region, respectively. $y_{i\mathrm{G}}$ is also the normal distance of atom i from the middle of the ribbon.

$H_{\mathrm{CR(CL)}}$ also shows the Hamiltonian for the coupling between the central region with the right (left) lead and using the TB approximation can be written as

$$H_{\mathrm{CR(CL)}} = -t_{\mathrm{CR(CL)}} \sum_{\langle i,j\rangle,\alpha} c_{i\alpha}^{\dagger} c_{j\alpha} + \mathrm{H.c.}, \tag{4}$$

where $t_{\mathrm{CR(CL)}}$ represents the hopping energy between the central region and right (left) lead. The contact hopping energy can also be determined by averaging the values obtained from the Harrison's scaling law[67,68]. In this study, namely, the hopping energies are re-calculated for the GE and SE at the interface when the C and Si atoms bond-lengths are changed to 1.8 Å. The geometric mean of the obtained hopping energy values (i.e., 2.07 eV) will then be used as the $t_{\mathrm{CR(CL)}}$ parameter, which is required to be the same order of $t_{\mathrm{R(L)}}$ and t_{C}[55]. The electronic transport is assumed ballistic. Such an assumption is valid when the mean free path of the carriers, which is in the order of the micron in the SE and GE at room temperature, is larger than the sample dimensions. This is due to the high mobility of charge carriers in the SE and GE, and thus they can simply move long distances without inelastic scattering. In the central region, the spin direction of the electron is assumed preserved, and the spin-flip scattering is ignored. Thus, the spin-up and spin-down electron transports can individually be studied. This assumption is correct because the spin diffusion length in the SE is in the order of several micrometers[29,69].

To determine the spin-dependent current, it is first required the spin-dependent electron transmission function to be calculated. The Green's function of the central region can be written as follows[70]:

$$G_{\mathrm{C},\alpha} = \left[(E + \mathrm{i}0^{+})\mathrm{I} - \mathrm{H_C} - \sum\nolimits_{\mathrm{L},\alpha} - \sum\nolimits_{\mathrm{R},\alpha}\right]^{-1}, \tag{5}$$

where $\Sigma_{\mathrm{R(L)},\alpha}$ is the right (left) self-energy matrix and is computed by Eq. (6). $\Sigma_{\mathrm{R(L)},\alpha}$ includes the effect of two semi-infinite AGNRs on the central region.

$$\sum\nolimits_{\mathrm{R},\alpha} = H_{\mathrm{CR}} g_{\mathrm{R},\alpha}(E) H_{\mathrm{CR}}^{\dagger}, \tag{6a}$$

$$\sum\nolimits_{\mathrm{L},\alpha} = H_{\mathrm{LC}}^{\dagger} g_{\mathrm{L},\alpha}(E) H_{\mathrm{LC}}, \tag{6b}$$

in which, $g_{\mathrm{R(L)},\alpha}$ is the surface Green's function of the right (left) lead and is computed by

$$g_{\mathrm{R(L)},\alpha}(E) = \left[(E + \mathrm{i}0^{+})\mathrm{I} - \mathrm{H}_{\mathrm{R(L)}}^{00} - \mathrm{H}_{\mathrm{R(L)}}^{01(\dagger)} \mathrm{T}_{\mathrm{R(L)}}\right]^{-1}, \tag{7}$$

where $H_{\mathrm{R(L)}}^{00}$ defines the TB Hamiltonian matrix of the unit cell studied in this research for the right (left) lead. $H_{\mathrm{R(L)}}^{01(\dagger)}$ is the hopping matrix between two adjacent unit cells in the right (left) lead. $T_{\mathrm{R(L)}}$ is the transfer matrix of the right (left) lead and can be determined using an iterative methodology, as proposed in Reference[70]. The electron transmission function can then be obtained using the following equations[70]:

$$T_{\alpha}(E) = Tr\left[\Gamma_{\mathrm{L},\alpha}(E) \mathrm{G}_{\mathrm{C},\alpha}(E) \Gamma_{\mathrm{R},\alpha}(E) G_{\mathrm{C},\alpha}^{\dagger}(E)\right], \tag{8}$$

where $\Gamma_{\mathrm{R(L)},\alpha}$ is the broadening function and describes the coupling between the right (left) lead with the central region.$\Gamma_{\mathrm{R(L)},\alpha}$ is given by

$$\Gamma_{\mathrm{R(L)},\alpha} = \mathrm{i}\left(\sum\nolimits_{\mathrm{R(L)},\alpha} - \sum\nolimits_{\mathrm{R(L)},\alpha}^{\dagger}\right). \tag{9}$$

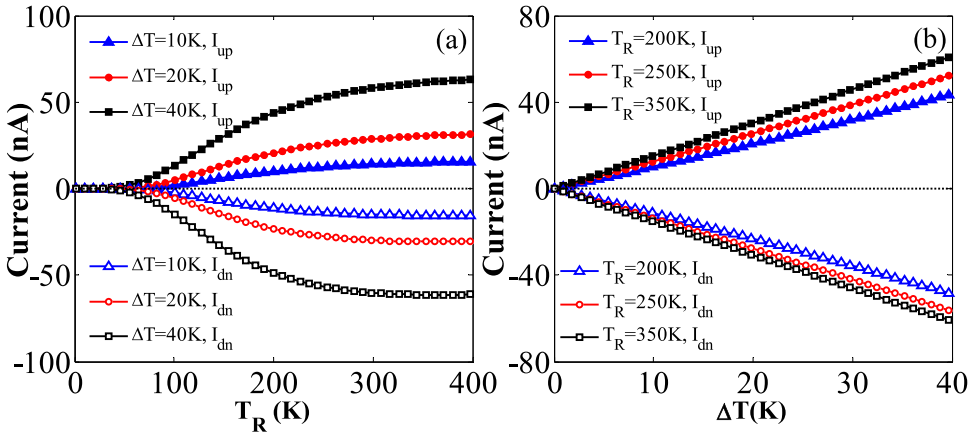

Figure 2. The thermally-induced spin currents for the considered hybrid GSNRs (**a**) the variation of the spin currents versus the right lead temperature, T_R, for different temperature gradients, $\Delta T = 10$, 20, and 40 K. The spin-up (I_{up}) and spin-down (I_{dn}) currents flow in positive and negative directions, respectively (i.e., SSE) (**b**) the variation of the spin currents versus ΔT for the right lead temperatures $T_R = 200$, 250, and 350 K.

Spin-dependent thermoelectric. The thermally-induced spin-dependent electric current can be computed by using the Landauer-Büttiker expression, as follows[71]:

$$I_\alpha = \frac{e}{h}\int_{-\infty}^{+\infty} T_\alpha(E)[f_L(E,T_L) - f_R(E,T_R)]dE, \tag{10}$$

where $f_{R(L)}$ is the Fermi–Dirac distribution. e, h, and $T_{R(L)}$ are also the electron charge, Plank constant, and temperature of the right (left) lead, respectively. As shown in Eq. (10), the temperature gradient $\Delta T = T_L — T_R$ between the leads produces a nonzero value of $f_L — f_R$, and thus the spin-dependent current is simply identified as a function of ΔT and $T_{R(L)}$. The net spin and charge currents can then be obtained by $I_S = I_{up} - I_{dn}$ and $I_C = I_{up} + I_{dn}$, respectively. To compute the other spin-dependent thermoelectric quantities, an intermediate function can be defined as follows[71]:

$$L_{n,\alpha}(E_F, T) = -\frac{1}{h}\int (E - E_F)^n \frac{\partial f(E, E_F, T)}{\partial E} T_\alpha(E)dE, \tag{11}$$

where E_F and T are the Fermi Energy and temperature values, respectively. Assuming a linear response regime, $\Delta T \cong 0$, the other spin-dependent thermoelectric parameters such as the spin-dependent thermopower, electrical conductance, and the electron's contribution to the thermal conductance can be calculated[72]. Based on Eq. (11), the spin-dependent Seebeck coefficient can then be calculated as follows:

$$S_\alpha = -\frac{1}{eT}\left(\frac{L_{1\alpha}}{L_{0\alpha}}\right). \tag{12}$$

where $S_S = S_{up} — S_{dn}$ and $S_C = (S_{up} + S_{dn})/2$ are the spin and charge Seebeck coefficients, respectively[72].

Results and discussion

In this section, the results of the current study are presented and discussed. For this purpose, Eqs. (8) and (10), along with the intermediate function, have been used to evaluate the obtained results. A hybrid nanoribbon system is first defined and then subjected to different local external fields, including the perpendicular electric (E_Z) and ferromagnetic exchange (M_z) fields, which are applied to the central region (see Fig. 1). The application of the local external electric[73] and ferromagnetic exchange fields are now experimentally feasible. For example, a ferromagnetic exchange field can be created by the proximity with a ferromagnetic insulator EuO as suggested for GE[74]. An inhomogeneous transverse electric field with the magnitude of E_{yS} and E_{yG} are also applied to the device, the left and right leads, respectively[75]. The electric current obtained by the temperature difference (ΔT) without any external bias voltage, i.e., the difference between the temperature of the left, T_L, and the right, T_R, leads are calculated.

Spin-dependent seebeck effect. In order to study the thermal spin transport properties of the considered hybrid GSNRs, the values of the spin-up (I_{up}) and spin-down (I_{dn}) currents are determined as a function of T_R for three different temperature gradients $\Delta T = 10$, 20, and 40 K (see Fig. 2). The values of $M_z = 0.181$ eV, $E_z = 0.081$ V/Å, $E_{yS} = 0.127$ V/Å, and $E_{yG} = 0.913$ V/Å are selected, and a positive spin-up and negative spin-down currents are evidently observed. These values have been selected based on the previous studies (e.g.,[76–79]), and it is believed that they can provide relatively large symmetric spin currents. A nearly perfect SDSE is identified in this hybrid GSNRs[14,15,80]. Because the spin-up and spin-down currents have only produced due to the temperature

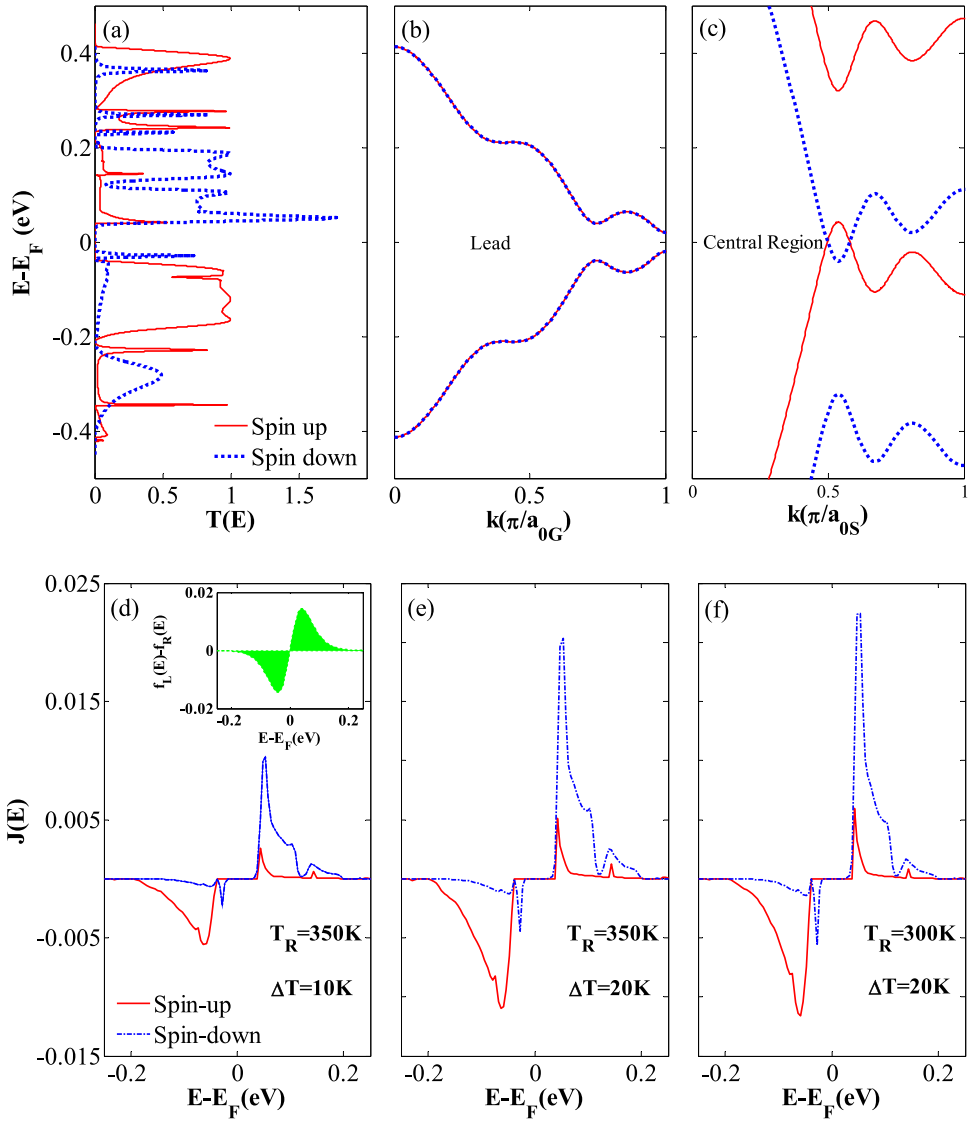

Figure 3. (**a**) The spin-dependent transmission spectra (T_{up} and T_{dn}) versus $E-E_F$, (**b**) the band structures of the right (left) lead with an applied electric field of $E_{yG}=0.913$ V/Å, (**c**) the band structures of the ferromagnetic central region including an exchange field of $M_z=0.181$ eV, electric fields of $E_Z=0.081$ V/Å and $E_{yS}=0.127$ V/Å, and the variation of the spin-dependent current spectrum $J(E)$ versus $E-E_F$ for (**d**) $T_R=350$ and $\Delta T=10$ K, (inset shows the difference between the Fermi–Dirac distributions for the left and right leads, $f_L(E)$-$f_R(E)$, as a function of $E-E_F$), (**e**) $T_R=350$ and $\Delta T=20$ K, and (**f**) $T_R=300$ and $\Delta T=20$ K.

gradient, and they flow in opposite directions with almost equal magnitudes. The GSNR evidently shows a good insulating behavior without any charge or spin current for the low-temperature values. As shown in Fig. 2(a), the threshold temperatures of $T_{th}=60$, 50, and 40 K are almost obtained for $\Delta T=10$, 20, and 40 K, respectively; where the spin-up and spin-down currents are almost zero for $T_R<T_{th}$, whereas the spin currents proportionally increase with respect to T_R for $T_R>T_{th}$. The spin currents also increase in opposite directions as ΔT increases (see Fig. 2b) such that they vary linearly and symmetrically respect to the zero-current axis for the entire range of ΔT.

The SDSE is further confirmed by all these issues. It is worth mentioning that the studied hybrid GSNRs can significantly provide larger thermally-induced spin currents compared to those given by the pristine AGNRs and ZSNRs.

In order to well understand the SDSE phenomenon in the considered hybrid GSNRs, the Landauer Büttiker formula (Eq. 10) is studied in detail. As can be seen from Eq. (10), the transport coefficients and the difference between the Fermi–Dirac distributions of the left (f_L) and right (f_R) electrodes provide the two factors affecting the thermal spin-dependent currents. Because the leads are composed of similar material and density of states, the difference in carrier concentrations between these two leads is due to the temperature difference and is calculated using the Fermi–Dirac distribution. It is noted that f_L-f_R is an odd function around the Fermi level, and thus the sign of the current function is determined by the slope of the transmission coefficients for this region. f_L-f_R is almost equal to zero for the higher energy values (see the inset of Fig. 3d)[10]. As the carriers with the energies

higher (lower) than the Fermi level flow from the left (right) lead towards the right (left) lead, the electron, $I_e<0$ (hole, $I_h>0$) currents are generated, respectively. A net zero thermal current is obtained when the transmission spectrum is symmetric, and I_e and I_h currents neutralize each other. The variations of the spin-dependent transmission coefficients (T_{up} and T_{dn}) versus the energy $E–E_F$ around the Fermi level (here E_F is set to zero) are shown in Fig. 3(a). As shown in Fig. 3(a), because the spin-up and spin-down transmission spectra have been located below and above the Fermi level, I_{up} and I_{dn} will also have opposite signs.

Two narrow transmission bands for the spin-up and spin-down electrons almost occur within the range of -0.2 eV $< E–E_F < -0.04$ eV and 0.04 eV $< E-E_F <$ 0.2 eV, respectively (see Fig. 3a). It is worth mentioning that the electron–hole symmetry is often disturbed by these transmission peaks and result in a nonzero net spin current[81]. For further explanation, the peak value of the spin-down electron transmission has been located above the Fermi level, and thus the electrons can be transported from the right lead to the left one. This leads to a negative spin-down current. On the contrary, because the peak value of the spin-up electron transmission occurs below the Fermi level, the transport of holes produces a positive spin-up current from the left lead to the right one (see Fig. 3a). There also exist two peak values for the spin-up and spin-down electrons in the above and below the Fermi level. However, compared to the former peak values, they are very small. Accordingly, a nearly perfect SDSE is observed in the hybrid GSNRs, because the transmission peaks for the spin-up and spin-down electrons are almost symmetric relative to the Fermi level. In this study, a relatively moderate threshold temperature T_{th} (~ 50 K) for each spin current is needed to extend the Fermi distribution and cover the transmission peaks. This causes a nonzero spin current to be produced between the left and right leads. All these issues may be attributed to the fact that the Fermi distribution is exponentially decreased, and the transmission spectrum shows a relatively medium energy gap for the spin-up and spin-down electrons.

To assess the combined effects of external fields on the hybrid GSNRs, the band structures of the leads and central region are also shown in Fig. 3(b),(c). The lowest-energy subbands for each band structure are related to the electron and hole for $E-E_F>0$ and $E-E_F<0$, respectively. As shown in Fig. 3(b), the spin-dependent subbands of the leads are almost matched, whereas the lowest-energy subbands of the central region belong to two different spin states (see Fig. 3c). The effects of each external field are (1) the ferromagnetic exchange field ($M_z=0.181$ eV) causes different spins to shift in opposite directions and lead to a huge spin splitting[74]. In other words, the proximity effect causes the gapless spin edge states are damaged (2) the semiconducting gaps are also generated between the hole and electron subbands when a perpendicular electric field ($E_z=0.081$ V/Å) is applied[41]. This is due to the fact that the inversion symmetry is broken by the staggered sublattice potential (3) the transverse electric field ($E_{yS}=0.127$ V/Å and $E_{yG}=0.913$ V/Å) produces the gaps between the hole and electron subbands, and causes the electron states to shift to the lower energies, whereas the hole states shift to the higher ones[82]. The band structure shown in Fig. 3(b),(c) is obtained when all these fields are applied simultaneously.

Figure 3(d)–(f) show the current spectrum $J=T(f_L-f_R)$ of the spin currents, plotted for different temperature sets. The area limited to the current spectrum curve and the energy axis ($E-E_F$) defines the spin current (i.e., I_{up} and I_{dn}). As shown in Fig. 3(d)–(f), the spin-up current spectra are relatively symmetric with respect to the spin-down ones about the Fermi level and with almost equal areas for the entire different temperature sets. A comparison between the exact areas obtained from the current spectrum (J) for the spin-up and spin-down clearly shows that there is a very small difference between the spin-up and spin-down areas in each plot. This again confirms the nearly perfect SDSE. For I_{up}, the peak value of the current spectrum at $\Delta T=20$ K is larger than that of $\Delta T=10$ K when T_R is assumed equal to 350 K. This clearly shows that the spin current grows as ΔT increases. Nonetheless, the area under the J curves for $T_R=300$ K is smaller than that of $T_R=350$ K when ΔT is assumed to be 20 K. This indicates that the spin currents grow with the increase of T_R. Because, there is a bandgap in the transmission spectrum, a zero J value is also observed around the Fermi level.

The thermal-driven net spin currents, I_S ($=I_{up}-I_{dn}$), and the total charge currents, I_C ($=I_{up}+I_{dn}$), are also calculated. In Fig. 4, I_S and I_C are plotted versus T_R and ΔT. As shown in Fig. 4(a),(c), I_S value is generally increased as T_R or ΔT values are increased. For example, I_S value is almost 70, 86, and 100 times larger than those of I_C for $T_R=400$ K and $\Delta T=10$, 20, and 40 K, respectively, which are much greater than those reported in[10,83]. Thus, the carrier transport through the hybrid nanostructure is controlled by the spin current.I_C also shows some interesting transport properties when T_R or ΔT increases. For example, I_C is zero for $T_R<T_{th}$ when ΔT is equal to 20 K (see Fig. 4c). I_C also drops to the negative values when T_R is larger than T_{th}. This indicates the appearance of a thermoelectric switcher. As T_R is further increased, I_C reaches to its peak value where the negative differential thermal resistance emerges[84]. Indeed, the NDTR occurs due to the competition between I_{up} and I_{dn} with opposite flowing directions. I_C also decreases to a zero value as T_R increases to a critical temperature value of $T_R=358$ K. This clearly confirms the emergence of the thermal-induced pure spin current. The flowing direction of I_C changes for $T_R>358$ K, because its sign gets reverse. The variations of I_C versus ΔT are also computed and plotted in Fig. 4(d). As shown in Fig. 4(d), I_C is negative for the smaller values of $T_R=200$ and 250 K, and different values of ΔT, whereas I_C is almost equal to zero for the relatively large values of $T_R=350$ K. The observed behaviors clearly confirm that the current of the hybrid GSNRs is appropriate for different device applications by selecting various device temperature sets.

Thermal spin-filtering effect. The thermal SFE without any threshold temperatures in the hybrid GSNRs is studied in this subsection. The effects of an electric field of E_z = 0.030 V/Å and an exchange field of M_z = 0.157 eV, applied perpendicularly to the central region of the hybrid GSNR are also investigated. The inhomogeneous transverse electric fields equal to $E_{yS}=0.575$ V/Å and $E_{yG}=0.029$ V/Å are also considered. Figure 5(a) shows the variations of the thermally-induced currents versus T_R for different values of ΔT. As shown in Fig. 5(a), larger values of I_{up} are obtained for the high temperatures, whereas I_{dn} is zero for the entire range of temperature as T_R increases. The nearly perfect thermal SFE is valid[11,12,83], and this evidently illustrates that the spin-up

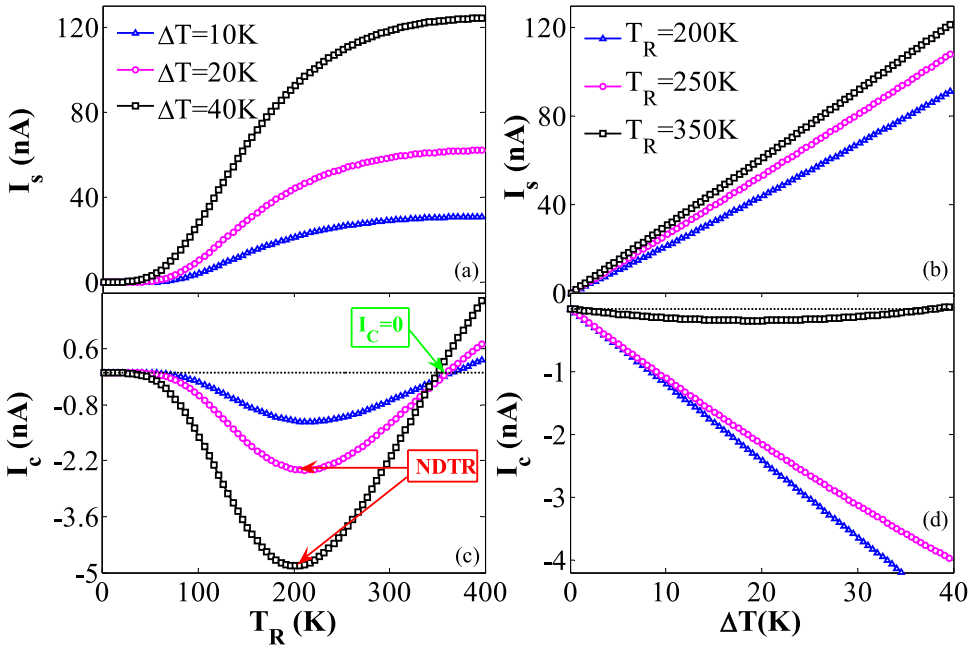

Figure 4. (**a**) The variation of the net spin current ($I_S = I_{up} - I_{dn}$) versus T_R for $\Delta T = 10$, 20, and 40 K, (**b**) the variation of I_S versus ΔT for $T_R = 200$, 250, and 350 K, (**c**) the total electron current ($I_C = I_{up} + I_{dn}$) as a function of T_R for $\Delta T = 10$, 20, and 40 K, and (**d**) the variation of I_C versus ΔT for $T_R = 200$, 250, and 350 K.

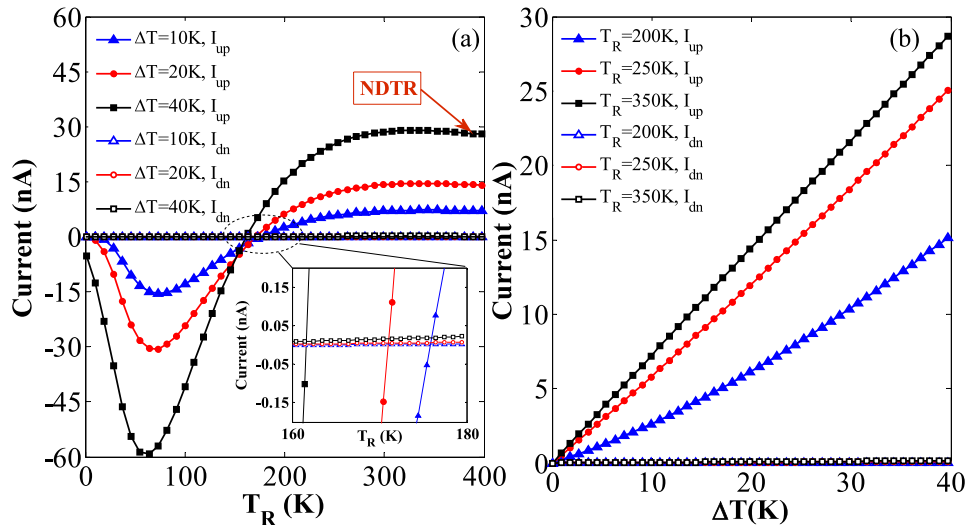

Figure 5. (**a**) The variations of the spin currents versus T_R for $\Delta T = 10$, 20, 40, the spin-up currents (I_{up}) have finite values and the spin-down currents (I_{dn}) are nearly zero (i.e., SFE), and (**b**) the spin currents versus ΔT for $T_R = 200$, 250, and 350 K.

transport channels are opened, whereas the spin-down transport channels always remain close. For example, I_{up} reaches to its maximum value and is then decreased to zero at a critical temperature value of $T_R = 172$ K and $\Delta T = 20$ K. However, I_{up} sign is reverse and the flowing direction is changed for $T_R > 172$ K. It is noted that when the I_{up} is maximum, the NDTR also reaches its peak value. Again, the NDTR occurs for the larger values of temperature and ΔT. As a result, the hybrid GSNR can be used as a thermal spin device with various multiple attributes. Figure 5(b) also shows the variations of I_{up} and I_{dn} versus ΔT for different values of $T_R = 200$, 250, and 350 K. As shown in Fig. 5(b), I_{up} increases when T_R and ΔT are increased, whereas I_{dn} remains almost zero for different values of ΔT. This further confirms that the SFE has been produced.

The spin-dependent transmission spectrum is also displayed in Fig. 6(a). As shown in Fig. 6(a), the first peak value of the spin-up transmission occurs in the energy values ranging from 0 to 0.03 eV, whereas the second peak value occurs in the energy values ranging from −0.03 to −0.13 eV. Hence, the spin-up dominates the transport

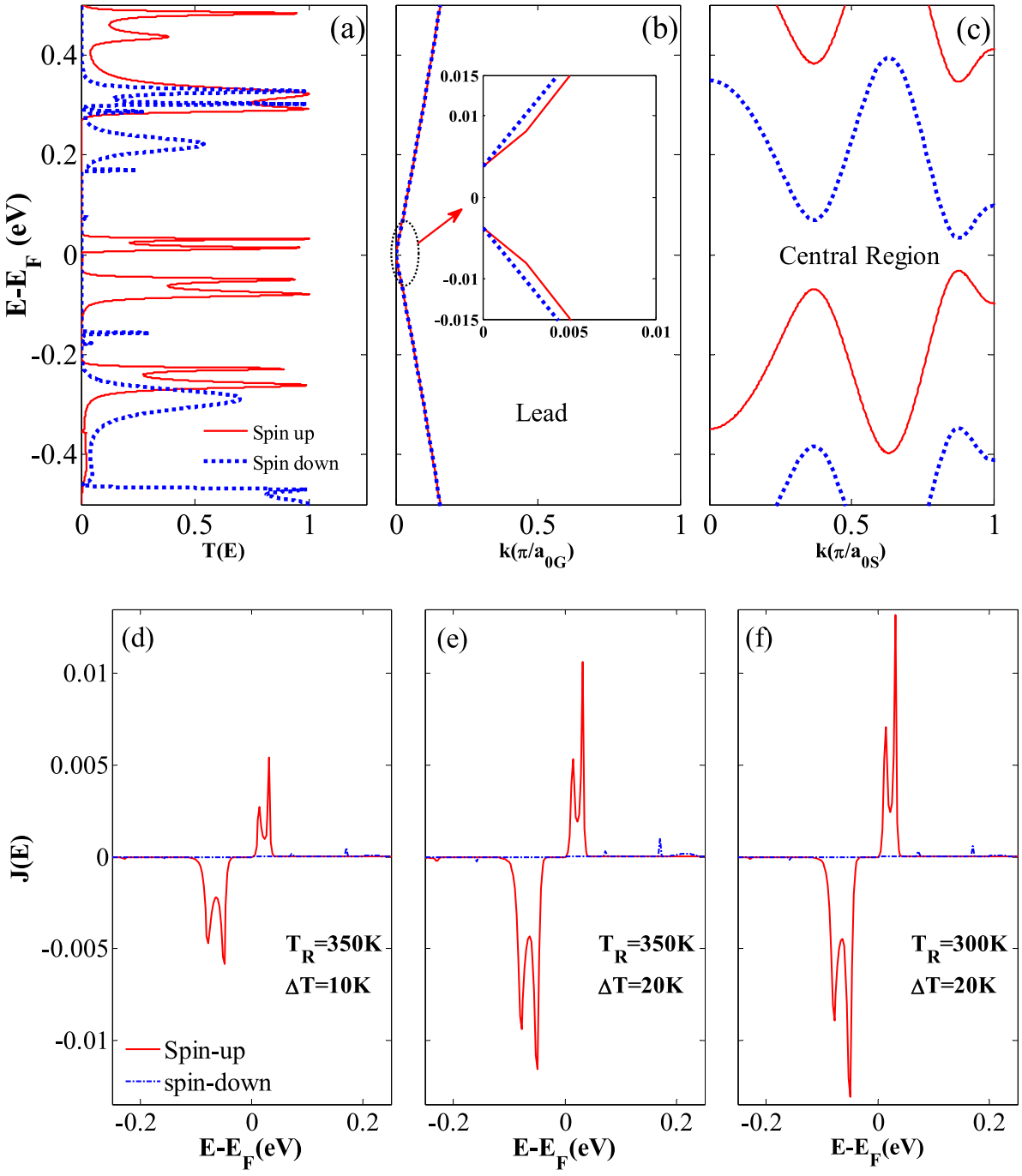

Figure 6. (**a**) The spin-dependent transmission spectra (T_{up} and T_{dn}) versus $E-E_F$, (**b**) the band structures of the right (left) lead with an applied electric field of $E_{yG}=0.029$ V/Å (inset shows the spin splitting induced by the electric field is very small and negligible) (**c**) the band structures of the ferromagnetic central region including an exchange field of $M_z=0.157$ eV, electric fields of $E_Z=0.030$ V/Å, and $E_{yS}=0.575$ V/Å, and the variation of the spin-dependent current spectrum $J(E)$ for (d) $T_R=350$ and $\Delta T=10$ K, (**e**) $T_R=350$ and $\Delta T=20$ K, and (**f**) $T_R=300$ and $\Delta T=20$ K.

properties and yields a nearly perfect SFE. However, the spin-down transmission is almost zero within this range of energies. Like in SDSE case, the combined effects of external fields on the hybrid GSNRs are also evaluated for the SFE case and similar results are obtained. Figure 6(b),(c) shows the band structures of the leads and central region for the considered hybrid GSNRs, respectively. As shown in Fig. 6(b), the spin-dependent subbands of the leads are almost matched, whereas the lowest-energy subbands of the central region belong to two different spin states (see Fig. 6c). As can be seen from Fig. 6(c), the ferromagnetic exchange field ($M_z = 0.157$ eV) causes different spins to shift in opposite directions. The semiconducting gaps are also generated between the hole and electron subbands when a perpendicular and/or transverse electric fields ($E_z = 0.030$ V/Å, $E_{yS}=0.575$ V/Å and $E_{yG}=0.029$ V/Å) are applied. However, the transverse electric field causes the electron states to shift to the lower

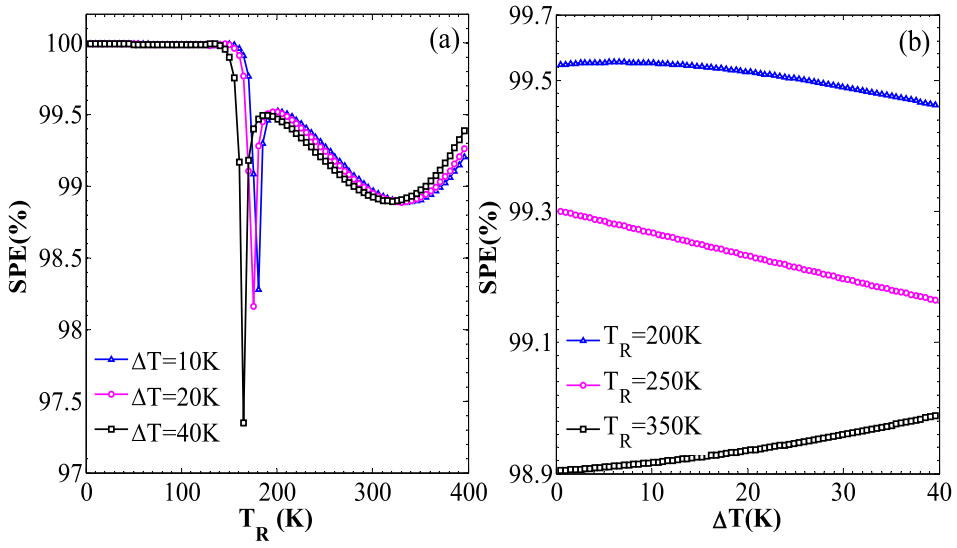

Figure 7. (**a**) The variation of the spin polarization efficiency (SPE) versus T_R for $\Delta T = 10$, 20, and 40 K (**b**) the SPE variation versus ΔT for $T_R = 200$, 250, and 350 K.

energies, whereas the hole states shift to the higher ones. It is noted that the spin splitting induced by the external electric field is very small and negligible, as shown in inset of Fig. 6(b). Figure 6(d),(f) show the current spectrum of the spin currents, plotted for different temperature sets. A comparison between the current spectrum of spin-up and spin-down clearly shows that the spin-down spectra are almost zero. However, the spin-up current spectra are dominant in all cases. This again confirms the nearly perfect SFE. For I_{up}, the peak value of the current spectrum at $\Delta T = 20$ K is larger than that of $\Delta T = 10$ K when T_R is assumed equal to 350 K. This confirms that the spin current is increased as ΔT increases. The J area for $T_R = 300$ K is smaller than that of $T_R = 350$ K when ΔT is assumed as 20 K. This shows that the increase of T_R increases the spin currents.

Figure 7 show the variations of spin polarization efficiency, SPE (%) $= (|I_{up}| - |I_{dn}|)/ (|I_{up}| + |I_{dn}|) \times 100$, versus T_R and ΔT, respectively. The results clearly show that a high SPE is achieved for the selected T_R values. For example, the SPE is almost equal to 100% for the low temperature values, whereas it is measured about 99% for a wide range of T_R and ΔT values[12,85]. It is noted that a numerical fluctuation for the T_R values ranging from 140 to 190 K is also observed. This basically is related to the reverse sign of I_{up} and the mutual competition between I_{up} and I_{dn} in this range of temperatures, as shown in inset of Fig. 5(a). It is noted that the spin channels of the pristine AGNRs and ZSNRs are partly conductive and the magnitude of the associated SPE is much less than that of the considered hybrid structure.

The effects of central region length. In this subsection, the effects of central region length (L) on the thermally-induced current for the considered hybrid ZGSNRs is studied. The variations of the spin currents (I_{up} and I_{dn}) versus T_R at $\Delta T = 40$ K for $M = 7$–13, and selected external fields has been shown in Fig. 8(a), in the SDSE case. Indeed, the L parameter proportionally changes with M, in all cases. According to Fig. 8(a), SDSE occurs for $M = 8$, 9, 12, and 13 for a wide range of T_R values around the room temperature (see the filled darker points). However, $M = 8$ was selected in this research because it can provide a perfect SDSE and stronger spin currents. Figure 8(b) also shows the changes of I_S and I_C versus M at $T_R = 300$ K and $\Delta T = 40$ K. As shown in Fig. 8(b), I_S is two order of magnitude (i.e., they differ by a factor ranging from 10 to 100) larger than I_C for some M values (see darker filled points). This again confirms that $M = 8$ can suitably provide the largest I_S value and a stronger SDSE for the selected external fields. Figure 8(c) shows the variations of the spin currents versus T_R at $\Delta T = 40$ K for $M = 7$–13 and the adopted external fields, in the SFE case. It is realized that the I_{up} is relatively enhanced for $M = 8$ and leads to a larger thermal-induced spin current and a stronger thermal SFE in the hybrid ZGSNRs. Figure 8(d) also provides evidence that the I_{up} (I_{dn}) is two order of magnitude larger than I_{dn} (I_{up}) for some M values at $T_R = 300$ K and $\Delta T = 40$ K, in the SFE case (see darker filled points). It is noted that the results reported in this section are all limited to the considered range of parameters and thus they cannot be generalized for various values of external fields.

Thermoelectric performance. The Seebeck coefficients for two different configurations of ferromagnetic exchange and local external electric fields, as discussed above, are studied in this section. Figure 9 shows the variations of the spin-up (S_{up}) and spin-down (S_{dn}) Seebeck coefficients, namely, the spin (S_S) and charge (S_C) Seebeck coefficients versus the Fermi energy. The SDSE and SFE are obtained for the hybrid GSNRs for the selected values of exchange and electric fields, as shown in Fig. 9(a),(b), respectively. In order to balance the thermal forces acting on the charge carriers, a larger bias for the lower electric conductance is often required. This consequently produces larger S_S values[86,87]. Different behaviors are generally observed for the S_{up} and S_{dn} of the two studied configurations. This is especially true for the E_F values ranging from −0.2 to 0.2 eV. In the SFE case,

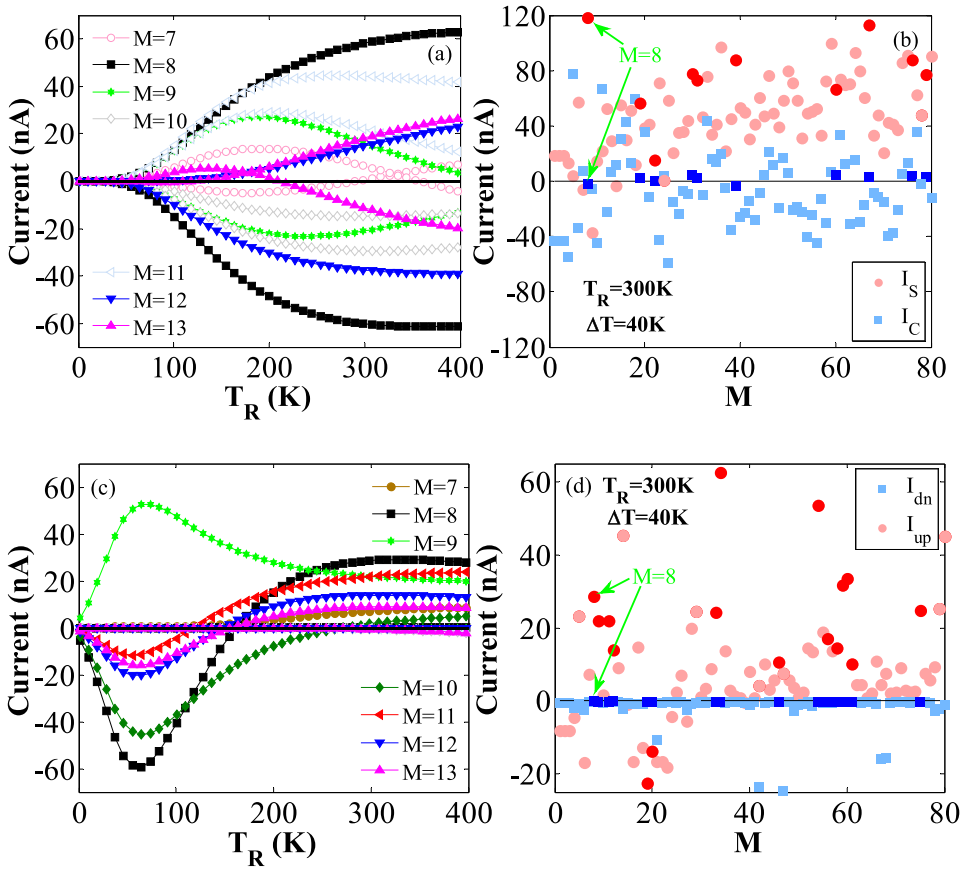

Figure 8. The variations of (**a**) I_{up} and I_{dn} versus T_R at $\Delta T = 40$ K for the lengths of $M = 7$–13; Note that the plots shown in the positive and negative regions of the Y-axis are related to I_{up} and I_{dn}, respectively, (**b**) I_S and I_C versus M at $T_R = 300$ K and $\Delta T = 40$ K, and the selected external fields, in the SSE case, (**c**) I_{up} and I_{dn} versus T_R at $\Delta T = 40$ K for $M = 7$–13; Note that the plots on the X axis are related to I_{dn}, and the others to the I_{up} (**d**) I_{up} and I_{dn} versus M at $T_R = 300$ K and $\Delta T = 40$ K, and the adopted external fields, in the SFE case.

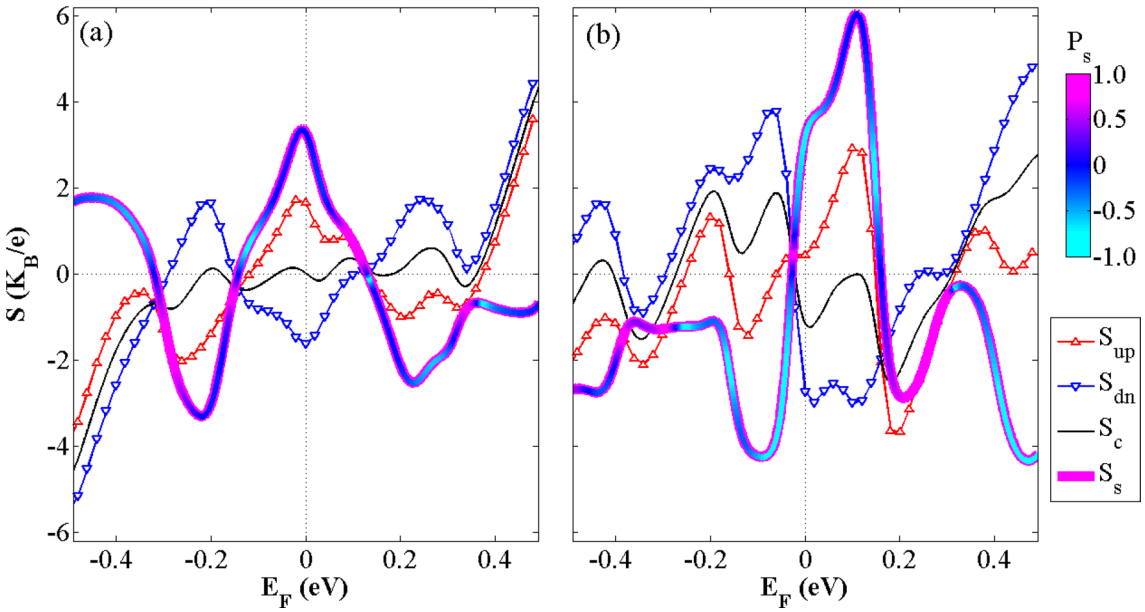

Figure 9. The variations of the spin-up (S_{up}), spin-down (S_{dn}), spin (S_s) and charge (S_c) Seebeck coefficients versus the Fermi energy and at room temperature for (**a**) the SSE and (**b**) the SFE cases. The S_S color changes in accordance with the Seebeck polarization value.

the peak values of − 3.67 and 3.77 for the S_{up} and S_{dn} are almost obtained for the $E_F = 0.20$ eV and $E_F = -0.06$ eV values, respectively (see Fig. 9), whereas these values for the SDSE are equal to 1.73 and − 2.0, and occur around the Fermi level. As can be seen from Fig. 9, when S_{up} is equal to zero for some values of the Fermi energy, S_{dn} is nonzero and vice versa. This is related to the fact that the electron and hole currents are canceled out by each other in one spin channel, whereas there is a thermally-induced spin-polarized current in the another one. For example, according to Fig. 9(b), in the SFE case, S_{up} values are almost equal to zero for $0.2 < E_F < 0.3$ eV, whereas S_{dn} has nonzero values in this range. It is worth mentioning that S_{up} equals to zero at three different points for the E_F values ranging from − 0.2 to 0.2 eV, whereas S_{dn} equals to zero at only one point in this region. As shown in Fig. 9, S_{up} and S_{dn} also have equal values with different signs at several E_F values. This results in zero S_C and nonzero S_S values in SDSE and SFE cases. It is noted that S_C slightly changes around the $S_C = 0$ line in the SDSE case (see Fig. 9a), whereas in the SFE case, it occurs at some different points (see Fig. 9b). This may be attributed to the fact that the S_{up} and S_{dn} are almost symmetric respect to this line. This shows that ΔT can produce a pure spin current without any charge current. Hence, a zero-charge voltage and a nonzero spin voltage ($V_S = S_S T$) are generated by the hybrid GSNRs[88]. The transport is created in such an issue by the spin-up holes and spin-down electrons with similar magnitudes but different current directions. Thus, ΔT can generate a pure spin current and a near-perfect SDSE. It is also observed that S_S is almost flat for the larger values of E_F. This may be due to the inversely symmetric relationship of the spin-dependent Seebeck coefficients and their linear dependence on the E_F. This leads to a constant difference between the S_{up} and S_{dn}. The Seebeck polarization, $P_S = (|S_{up}| - |S_{dn}|) / (|S_{up}| + |S_{dn}|)$ is also shown in Fig. 9 (see the thicker colored line) to separately specify the effect of each spin channel on the S_S. This is performed by changing the color of S_S as the P_S value is changed. As shown in Fig. 9, because S_{up} (S_{dn}) is almost dominant for some values of E_F, S_S color tends to magenta (turquoise) color in this region. However, because S_{up} and S_{dn} have almost equal values, but with different signs, the S_S color, almost tends to blue for the entire E_F values. It is worth mentioning that the S_{up} or S_{dn} signs are related to the *p*- or *n*-type nature of the device. S_S and S_C have the same sign when the S_{up} is dominant, whereas their signs are opposite as S_{dn} is dominant.

Figure 10 shows the variations of the spin Seebeck (S_s) and spin polarization (P_s) versus E_z and M_z for different values of the transverse electric fields. Various behaviors can be seen for the S_s and P_s parameters obtained from four different values of the transverse electric fields. As can be seen from the color bars in Fig. 10, the red and blue colors represent the large and small values for S_s and P_s, respectively. S_s and P_s are also considered as odd functions with respect to M_z for the entire plots[89]. This results in I_S direction can be tuned by changing the magnetization direction in the central region. This shows that I_S can magnetically be manipulated. Unlike E_z, S_s and P_s can significantly be changed by varying the exchange field. This further illustrates that S_s and P_s can magnetically be employed. It is noted that S_s and P_s are reach their peak values when M_z is almost equal to ± 0.1 eV, and with no transvers (or with homogeneous) electric fields. It is noted that these functions are even with respect to the E_z when $E_{yG} = E_{yS} = 0$ (Fig. 10(a),(b)). The results show that S_S increases when the absolute value of E_z is increased and $E_z < 0$ (see Fig. 10c), whereas the P_s can be large for the entire E_z values. However, the S_s value can almost be reached to ± 1 for the larger magnitudes of E_z. The maximum value of S_s almost occurs at $M_z = 0.1$ eV, as illustrated in Fig. 10(c). As shown in Fig. 10, P_S and S_S reach their peak values for a limited number of areas as the inhomogeneous transverse electric fields are adopted. S_S absolute maximum value is increased in SDSE and SFE cases as compared to the two previous cases (see Fig. 10e–h).

Figure 11 also shows the variations of the thermal-driven net spin current (I_S) and the total charge current (I_C) versus M_z and E_z at $T_R = 358$ K and $\Delta T = 20$ K (see Fig. 4c) for the SDSE case values of the transverse electric fields and in the absence of these fields. Different behaviors can be seen for the I_S and I_C parameters obtained from two plots. As can be seen from the color bars, the red and blue colors represent the large and small values for I_S and I_C, respectively. I_S is also considered as an odd function with respect to M_z for the entire plots i.e., I_S sign is varied by changing M_z sign. It is noted that these functions are even with respect to E_z when $E_{yG} = E_{yS} = 0$ (Fig. 11a,b). A pure spin current can be observed for a limited range of small and large values of M_z as I_S reaches its peak value, and $I_C = 0$. Figure 11(c),(d) also provides evidence that a pure spin current can be obtained as the M_z value is almost equal to 0.181 eV (see also Fig. 4c).

Conclusions

To realize the SDSE and the thermal SFE, the spin-dependent thermoelectric transport properties of hybrid GSNRs, as spin caloritronics devices, have been studied in this research. The effects of the temperature gradient between the left and right leads, ferromagnetic exchange fields, M_z, and the local external electric fields, E_z and E_y, were also included. The results showed that a nearly perfect SDSE could be observed in the hybrid GSNRs. Because the spin-up and spin-down currents are only produced due to the temperature gradient, and they flow in opposite directions with almost equal magnitudes. In the SDSE case, positive spin-up and negative spin-down currents with the threshold temperature T_{th} (~ 50 K) were observed for the values of $M_z = 0.181$ eV, $E_z = 0.081$ V/Å, $E_{yS} = 0.127$ V/Å, and $E_{yG} = 0.913$ V/Å. Different charge current behaviors have also been obtained by selecting various device temperature sets. A nearly zero charge thermopower was also obtained, which further demonstrates the emergence of the SDSE. In the SFE case, $M_z = 0.157$ eV, $E_z = 0.030$ V/Å, $E_{yS} = 0.575$ V/Å, and $E_{yG} = 0.029$ V/Å were considered. Larger values of the spin-up current were obtained for the high temperatures, whereas the spin-down current is zero for the entire range of temperatures as the right lead temperature (T_R) increases. Thus, a nearly perfect SFE was achieved at room temperature, whereas the spin polarization has reached up to 99%. It is noted that due to the competition between the spin-dependent currents, some interesting transport features such as the change of the flowing direction and negative differential thermoelectric resistance were observed. This evidently confirms the potential thermoelectric device applications of the studied hybrid

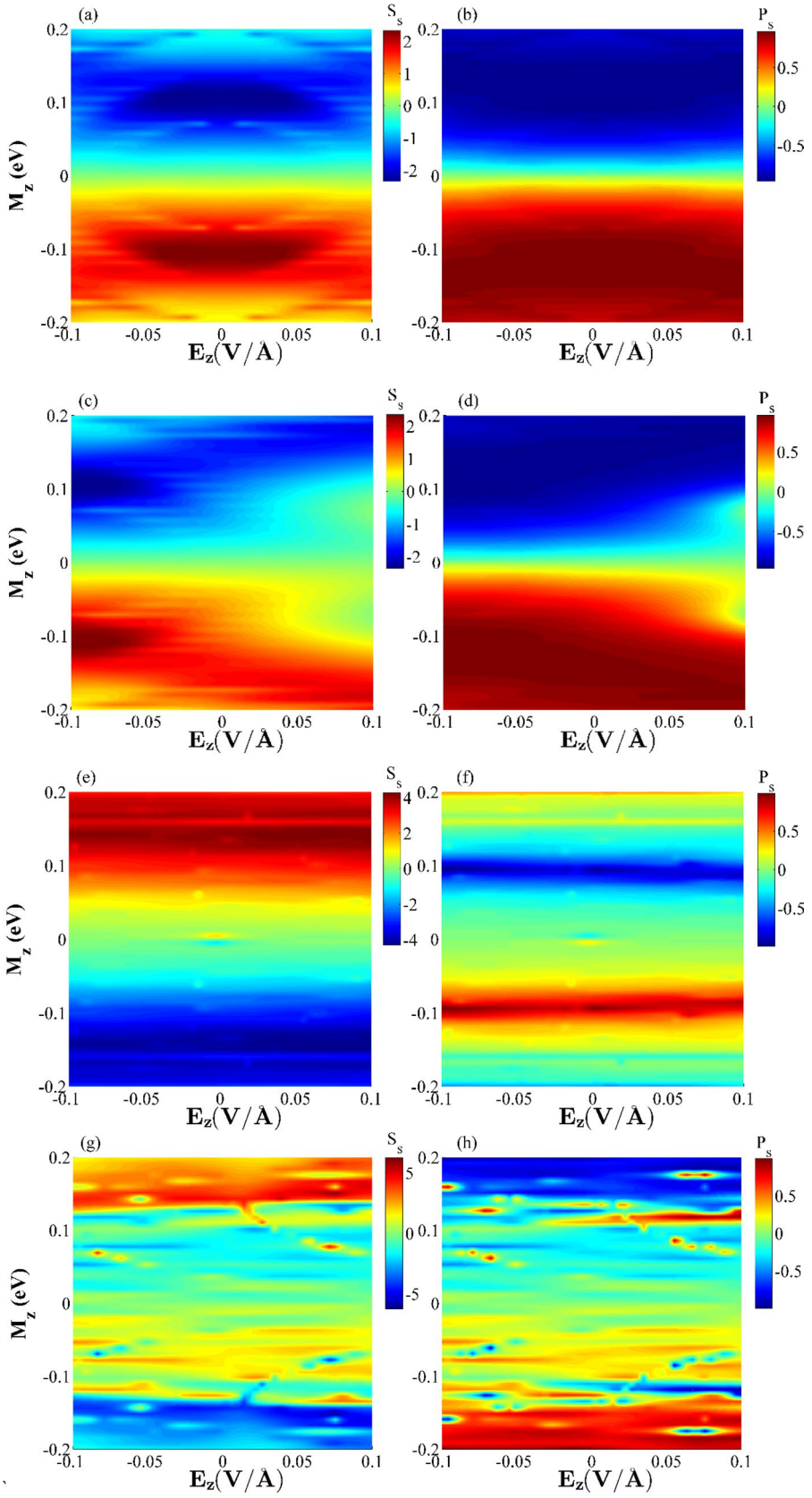

Figure 10. The combined effects of ferromagnetic exchange fields, M_Z, and external electric fields (E_Z, E_{yG} and E_{yS}) on the spin Seebeck coefficient (S_S) and Seebeck polarization (P_S) for the considered hybrid GSN*R* and (**a**,**b**) $E_{yG}=E_{yS}=0$ (**c**,**d**) $E_{yG}=E_{yS}=0.001$ V/Å (**e**,**f**) $E_{yG}=0.913$ V/Å, $E_{yS}=0.127$ V/Å (**g**,**h**) $E_{yG}=0.029$ V/Å, $E_{yS}=0.575$ V/Å. The scale of spin Seebeck coefficients in all plots is k_B/e.

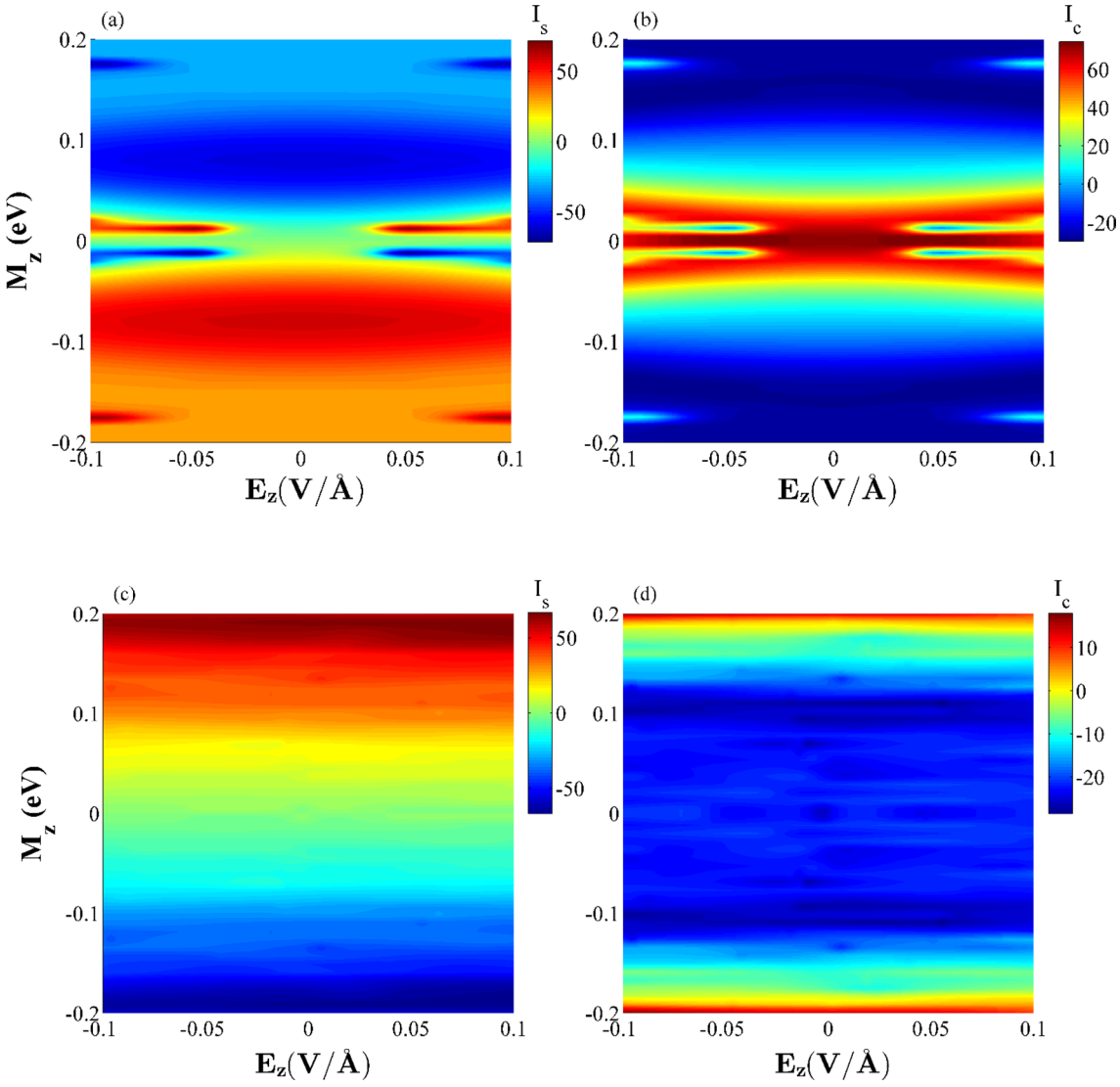

Figure 11. The combined effects of ferromagnetic exchange fields, M_z, and external electric fields (E_z and E_{yG}, E_{yS}) on the net spin current (I_S) and total electron current (I_C) for the considered hybrid GSNR and (**a**,**b**) $E_{yG} = E_{yS} = 0$ (**c**,**d**) $E_{yG} = 0.913$ V/Å, $E_{yS} = 0.127$ V/Å. The results are for $T_R = 358$ K and $\Delta T = 20$ K. I_S and I_C have nA units in all plots.

GSNRs by selecting various device temperature sets. The results reported and discussed in this study are limited to the considered set of parameters and thus they cannot be generalized for various values of external fields.

Received: 2 August 2020; Accepted: 23 December 2020
Published online: 08 January 2021

References

1. Bauer, G. E., Saitoh, E. & Van Wees, B. J. Spin caloritronics. *Nat. Mater.* **11**, 391–399 (2012).
2. Kirihara, A. *et al.* Spin-current-driven thermoelectric coating. *Nat. Mater.* **11**, 686–689 (2012).
3. Boona, S. R., Myers, R. C. & Heremans, J. P. Spin caloritronics. *Energy Environ. Sci.* **7**, 885–910 (2014).
4. Wolf, S. *et al.* Spintronics: a spin-based electronics vision for the future. *Science* **294**, 1488–1495 (2001).
5. Sanvito, S. Modeling Tools for Magnetism, Magnetic Materials, and Spintronics: Overview. In *Handbook of Materials Modeling: Methods: Theory and Modeling*, 837–840 (2020).
6. Hirohata, A. *et al.* Review on spintronics: Principles and device applications. *J. Magn. Magn. Mater.* https://doi.org/10.1016/j.jmmm.2020.166711 (2020).
7. Goennenwein, S. T. & Bauer, G. E. Spin caloritronics: Electron spins blow hot and cold. *Nat. Nanotechnol.* **7**, 145 (2012).
8. Nakabayashi, J., Yamamoto, D. & Kurihara, S. Band-selective filter in a zigzag graphene nanoribbon. *Phys. Rev. Lett.* **102**, 066803 (2009).
9. Uchida, K.-I. *et al.* Thermoelectric generation based on spin Seebeck effects. *Proc. IEEE* **104**, 1946–1973 (2016).
10. Fu, H.-H., Wu, D.-D., Zhang, Z.-Q. & Gu, L. Spin-dependent Seebeck effect, thermal colossal magnetoresistance and negative differential thermoelectric resistance in zigzag silicene nanoribbon heterojunciton. *Scientific reports* **5**, 10547 (2015).

11. Wu, D.-D., Du, G.-F. & Fu, H.-H. Spin-dependent Seebeck effect, and spin-filtering and diode effects in magnetic boron–nitrogen nanotube heterojunctions. *J. Mater. Chem. C* **8**, 4486–4492 (2020).
12. Wu, D.-D. *et al.* Thermal spin filtering, thermal spin switching and negative-differential-resistance in thermal spin currents in zigzag SiC nanoribbons. *Phys. Chem. Chem. Phys.* **16**, 17493–17498 (2014).
13. Kim, W. Y. & Kim, K. S. Prediction of very large values of magnetoresistance in a graphene nanoribbon device. *Nat. Nanotechnol.* **3**, 408 (2008).
14. Uchida, K. *et al.* Observation of the spin Seebeck effect. *Nature* **455**, 778–781 (2008).
15. Jaworski, C. *et al.* Observation of the spin-Seebeck effect in a ferromagnetic semiconductor. *Nat. Mater.* **9**, 898–903 (2010).
16. Bosu, S. *et al.* Spin Seebeck effect in thin films of the Heusler compound Co_2 MnSi. *Physical Review B* **83**, 224401 (2011).
17. Yarmohammadi, M. & Mirabbaszadeh, K. Enhancement of the anisotropic thermoelectric power factor of topological crystalline insulator SnTe and related alloys via external perturbations. *J. Mater. Chem. A* **7**, 25573–25585 (2019).
18. Wu, S. M., Pearson, J. E. & Bhattacharya, A. Paramagnetic spin Seebeck effect. *Phys. Rev. Lett.* **114**, 186602 (2015).
19. Wu, S. M. *et al.* Antiferromagnetic spin Seebeck effect. *Phys. Rev. Lett.* **116**, 097204 (2016).
20. Jaworski, C., Myers, R., Johnston-Halperin, E. & Heremans, J. Giant spin Seebeck effect in a non-magnetic material. *Nature* **487**, 210–213 (2012).
21. Kang, M.-S. *et al.* Large-scale MoS_2 thin films with a chemically formed holey structure for enhanced Seebeck thermopower and their anisotropic properties. *J. Mater. Chem. A* **8**, 8669–8677 (2020).
22. Zhu, L., Li, R. & Yao, K. Temperature-controlled colossal magnetoresistance and perfect spin Seebeck effect in hybrid graphene/boron nitride nanoribbons. *Phys. Chem. Chem. Phys.* **19**, 4085–4092 (2017).
23. Jiang, P. *et al.* Thermal spin current in zigzag silicene nanoribbons with sp 2–sp 3 edges. *RSC advances* **7**, 28124–28129 (2017).
24. Ghosh, S. *et al.* Dimensional crossover of thermal transport in few-layer graphene. *Nat. Mater.* **9**, 555–558 (2010).
25. Yousefi, F., Khoeini, F. & Rajabpour, A. Thermal conductivity and thermal rectification of nanoporous graphene: A molecular dynamics simulation. *Int. J. Heat Mass Transf.* **146**, 118884 (2020).
26. Lee, G.-H. *et al.* High-strength chemical-vapor-deposited graphene and grain boundaries. *Science* **340**, 1073–1076 (2013).
27. Ma, Y., Zhang, S., Xu, Y., Liu, X. & Luo, S.-N. Effects of temperature and grain size on deformation of polycrystalline copper–graphene nanolayered composites. *Phys. Chem. Chem. Phys.* **22**, 4741–4748 (2020).
28. Xu, X., Gabor, N. M., Alden, J. S., van der Zande, A. M. & McEuen, P. L. Photo-thermoelectric effect at a graphene interface junction. *Nano Lett.* **10**, 562–566 (2010).
29. Novoselov, K. S. *et al.* Two-dimensional gas of massless Dirac fermions in graphene. *Nature* **438**, 197–200 (2005).
30. Meyer, J. C. *et al.* The structure of suspended graphene sheets. *Nature* **446**, 60–63 (2007).
31. Tombros, N. *et al.* Anisotropic spin relaxation in graphene. *Phys. Rev. Lett.* **101**, 046601 (2008).
32. Chico, L., Orellana, P., Rosales, L. & Pacheco, M. Spin and charge caloritronics in bilayer graphene flakes with magnetic contacts. *Phys. Rev. Appl.* **8**, 054029 (2017).
33. Liu, Q.-B., Wu, D.-D. & Fu, H.-H. Edge-defect induced spin-dependent Seebeck effect and spin figure of merit in graphene nanoribbons. *Phys. Chem. Chem. Phys.* **19**, 27132–27139 (2017).
34. Takeda, K. & Shiraishi, K. Theoretical possibility of stage corrugation in Si and Ge analogs of graphite. *Phys. Rev. B* **50**, 14916 (1994).
35. Feng, B. *et al.* Evidence of silicene in honeycomb structures of silicon on Ag (111). *Nano Lett.* **12**, 3507–3511 (2012).
36. Meng, L. *et al.* Buckled silicene formation on Ir (111). *Nano Lett.* **13**, 685–690 (2013).
37. Aierken, Y., Leenaerts, O. & Peeters, F. M. A first-principles study of stable few-layer penta-silicene. *Phys. Chem. Chem, Phys.* **18**, 18486–18492 (2016).
38. Cahangirov, S., Topsakal, M., Aktürk, E., Şahin, H. & Ciraci, S. Two-and one-dimensional honeycomb structures of silicon and germanium. *Phys. Rev. Lett.* **102**, 236804 (2009).
39. Tao, L. *et al.* Silicene field-effect transistors operating at room temperature. *Nat. Nanotechnol.* **10**, 227–231 (2015).
40. Liu, C.-C., Feng, W. & Yao, Y. Quantum spin Hall effect in silicene and two-dimensional germanium. *Phys. Rev. Lett.* **107**, 076802 (2011).
41. Drummond, N., Zolyomi, V. & Fal'Ko, V. Electrically tunable band gap in silicene. *Phys. Rev. B* **85**, 075423 (2012).
42. Mahdavifar, M. & Khoeini, F. Highly tunable charge and spin transport in silicene junctions: phase transitions and half-metallic states. *Nanotechnology* **29**, 325203 (2018).
43. Khalkhali, M., Khoeini, F. & Rajabpour, A. Thermal transport in silicene nanotubes: Effects of length, grain boundary and strain. *Int. J. Heat Mass Transf.* **134**, 503–510 (2019).
44. Khalkhali, M., Rajabpour, A. & Khoeini, F. Thermal transport across grain boundaries in polycrystalline silicene: A multiscale modeling. *Sci. Rep.* **9**, 1–12 (2019).
45. Tan, X.-Y., Wu, D.-D., Liu, Q.-B., Fu, H.-H. & Wu, R. Spin caloritronics in armchair silicene nanoribbons with sp3 and sp2-type alternating hybridizations. *J. Phys.: Condens. Matter* **30**, 355303 (2018).
46. Zeng, M., Feng, Y. & Liang, G. Graphene-based spin caloritronics. *Nano Lett.* **11**, 1369–1373 (2011).
47. Balandin, A. A. *et al.* Superior thermal conductivity of single-layer graphene. *Nano Lett.* **8**, 902–907 (2008).
48. Hossain, M. S., Al-Dirini, F., Hossain, F. M. & Skafidas, E. High performance graphene nano-ribbon thermoelectric devices by incorporation and dimensional tuning of nanopores. *Sci. Rep.* **5**, 11297 (2015).
49. Zberecki, K., Wierzbicki, M., Barnaś, J. & Swirkowicz, R. Thermoelectric effects in silicene nanoribbons. *Phys. Rev. B* **88**, 115404 (2013).
50. Yang, X. *et al.* Temperature-controlled giant thermal magnetoresistance behaviors in doped zigzag-edged silicene nanoribbons. *RSC Adv.* **4**, 48539–48546 (2014).
51. Hicks, L. & Dresselhaus, M. S. Effect of quantum-well structures on the thermoelectric figure of merit. *Phys. Rev. B* **47**, 12727 (1993).
52. Wang, N., Han, L., He, H., Park, N.-H. & Koumoto, K. A novel high-performance photovoltaic–thermoelectric hybrid device. *Energy Environ. Sci.* **4**, 3676–3679 (2011).
53. Ohta, S., Nomura, T., Ohta, H. & Koumoto, K. High-temperature carrier transport and thermoelectric properties of heavily La-or Nb-doped $SrTiO_3$ single crystals. *J. Appl. Phys.* **97**, 034106 (2005).
54. Bansal, P. & Martin, A. Comparative study of vapour compression, thermoelectric and absorption refrigerators. *Int. J. Energy Res.* **24**, 93–107 (2000).
55. Zhang, Z., Xie, Y., Peng, Q. & Chen, Y. A theoretical prediction of super high-performance thermoelectric materials based on MoS2/WS2 hybrid nanoribbons. *Sci. Rep.* **6**, 21639 (2016).
56. Yang, K. *et al.* Enhanced thermoelectric properties in hybrid graphene/boron nitride nanoribbons. *Phys. Rev. B* **86**, 045425 (2012).
57. Liu, B. *et al.* Interface thermal conductance and rectification in hybrid graphene/silicene monolayer. *Carbon* **79**, 236–244 (2014).
58. Matthes, L., Hannewald, K. & Bechstedt, F. Ab initio investigation of graphene-based one-dimensional superlattices and their interfaces. *Phys. Rev. B* **86**, 205409 (2012).
59. Kistanov, A. A., Cai, Y., Zhang, Y.-W., Dmitriev, S. V. & Zhou, K. Strain and water effects on the electronic structure and chemical activity of in-plane graphene/silicene heterostructure. *J. Phys.: Condens. Matter* **29**, 095302 (2017).
60. Kiraly, B., Mannix, A. J., Hersam, M. C. & Guisinger, N. P. Graphene–silicon heterostructures at the two-dimensional limit. *Chem. Mater.* **27**, 6085–6090 (2015).

61. Li, G. *et al.* Stable silicene in graphene/silicene Van der Waals heterostructures. *Adv. Mater.* **30**, 1804650 (2018).
62. Drissi, L., Saidi, E., Bousmina, M. & Fassi-Fehri, O. DFT investigations of the hydrogenation effect on silicene/graphene hybrids. *J. Phys.: Condens. Matter* **24**, 485502 (2012).
63. Liu, B. *et al.* Interfacial thermal conductance of a silicene/graphene bilayer heterostructure and the effect of hydrogenation. *ACS Appl. Mater. Interfaces* **6**, 18180–18188 (2014).
64. Kimouche, A. *et al.* Ultra-narrow metallic armchair graphene nanoribbons. *Nat. Commun.* **6**, 10177 (2015).
65. Reich, S., Maultzsch, J., Thomsen, C. & Ordejon, P. Tight-binding description of graphene. *Phys. Rev. B* **66**, 035412 (2002).
66. Kane, C. L. & Mele, E. J. Quantum spin Hall effect in graphene. *Phys. Rev. Lett.* **95**, 226801 (2005).
67. Qasemnazhand, M., Khoeini, F. & Shekarforoush, S. Electronic transport properties in the stable phase of a cumulene/B 7/cumulene molecular bridge investigated using density functional theory and a tight-binding method. *New J. Chem.* **43**, 16515–16523 (2019).
68. Barrios-Vargas, J. E. *et al.* Electrical and thermal transport in coplanar polycrystalline graphene–hbn heterostructures. *Nano Lett.* **17**, 1660–1664 (2017).
69. 69Vogt, P. & Le Lay, G. *Silicene: Prediction, Synthesis, Application*. (Springer, 2018).
70. Khoeini, F., Khoeini, F. & Shokri, A. Peculiar transport properties in Z-shaped graphene nanoribbons: A nanoscale NOR gate. *Thin Solid Films* **548**, 443–448 (2013).
71. Sivan, U. & Imry, Y. Multichannel Landauer formula for thermoelectric transport with application to thermopower near the mobility edge. *Phys. Rev. B* **33**, 551 (1986).
72. Wu, D. *et al.* Pure spin current generated in thermally driven molecular magnetic junctions: A promising mechanism for thermoelectric conversion. *J. Mater. Chem. A* **7**, 19037–19044 (2019).
73. Le, P., Davoudiniya, M., Mirabbaszadeh, K., Hoi, B. & Yarmohammadi, M. Combined electric and magnetic field-induced anisotropic tunable electronic phase transition in AB-stacked bilayer phosphorene. *Physica E* **106**, 250–257 (2019).
74. Swartz, A. G., Odenthal, P. M., Hao, Y., Ruoff, R. S. & Kawakami, R. K. Integration of the ferromagnetic insulator EuO onto graphene. *ACS Nano* **6**, 10063–10069 (2012).
75. Tran, V.-T., Saint-Martin, J. & Dollfus, P. Large on/off current ratio in hybrid graphene/BN nanoribbons by transverse electric field-induced control of bandgap. *Appl. Phys. Lett.* **105**, 073114 (2014).
76. Correa, J. *et al.* Anisotropy of the spin-polarized edge current in monolayer transition metal dichalcogenide zigzag nanoribbons. *Phys. Rev. B* **101**, 195422 (2020).
77. Qiao, Z. *et al.* Quantum anomalous Hall effect in graphene proximity coupled to an antiferromagnetic insulator. *Phys. Rev. Lett.* **112**, 116404 (2014).
78. Li, H., Shao, J., Yao, D. & Yang, G. Gate-voltage-controlled spin and valley polarization transport in a normal/ferromagnetic/normal MoS2 junction. *ACS Appl. Mater. Interfaces* **6**, 1759–1764 (2014).
79. Zhang, Y. *et al.* Direct observation of a widely tunable bandgap in bilayer graphene. *Nature* **459**, 820–823 (2009).
80. Kajiwara, Y. *et al.* Transmission of electrical signals by spin-wave interconversion in a magnetic insulator. *Nature* **464**, 262–266 (2010).
81. Li, Z., Qian, H., Wu, J., Gu, B.-L. & Duan, W. Role of symmetry in the transport properties of graphene nanoribbons under bias. *Phys. Rev. Lett.* **100**, 206802 (2008).
82. Sisakht, E. T., Zare, M. H. & Fazileh, F. Scaling laws of band gaps of phosphorene nanoribbons: A tight-binding calculation. *Phys. Rev. B* **91**, 085409 (2015).
83. Wu, D.-D., Fu, H.-H., Liu, Q.-B., Du, G.-F. & Wu, R. Magnetic nanotubes: A new material platform to realize a robust spin-Seebeck effect and a perfect thermal spin-filtering effect. *Phys. Rev. B* **98**, 115422 (2018).
84. Li, B., Wang, L. & Casati, G. Negative differential thermal resistance and thermal transistor. *Appl. Phys. Lett.* **88**, 143501 (2006).
85. Zberecki, K., Swirkowicz, R., Wierzbicki, M. & Barnaś, J. Spin effects in thermoelectric phenomena in SiC nanoribbons. *Phys. Chem. Chem. Phys.* **17**, 1925–1933 (2015).
86. Zhou, B., Zhou, B. & Zeng, Y. Spin-dependent electronic and thermoelectric transport properties for a sawtoothlike graphene nanoribbon coupled to two ferromagnetic leads. *J. Low Temp. Phys.* **198**, 56–69 (2020).
87. Ouyang, Y. & Guo, J. A theoretical study on thermoelectric properties of graphene nanoribbons. *Appl. Phys. Lett.* **94**, 263107 (2009).
88. Cahaya, A. B., Tretiakov, O. A. & Bauer, G. Spin Seebeck power conversion. *IEEE Trans. Magn.* **51**, 1–14 (2015).
89. Yokoyama, T. Controllable valley and spin transport in ferromagnetic silicene junctions. *Phys. Rev. B* **87**, 241409 (2013).

Author contributions

Z.G.: writting, analysis. F.K.: Supervision, writing, verification.

Competing interests

The authors declare no competing interests.

Additional information

Correspondence and requests for materials should be addressed to F.K.

Reprints and permissions information is available at www.nature.com/reprints.

Publisher's note Springer Nature remains neutral with regard to jurisdictional claims in published maps and institutional affiliations.